# ORIGINAL PAPER

**S. Merkel · A. P. Jephcoat · J. Shu · H.-K. Mao**
**P. Gillet · R. J. Hemley**

# Equation of state, elasticity, and shear strength of pyrite under high pressure

**Abstract** Physical properties including the equation of state, elasticity, and shear strength of pyrite have been measured by a series of X-ray diffraction in diamond-anvil cells at pressures up to 50 GPa. A Birch–Murnaghan equation of state fit to the quasihydrostatic pressure–volume data obtained from laboratory X-ray source/film techniques yields a quasihydrostatic bulk modulus $K_{0T} = 133.5$ ($\pm 5.2$) GPa and bulk modulus first pressure derivative $K'_{0T} = 5.73$ ($\pm 0.58$). The apparent equation of state is found to be strongly dependent on the stress conditions in the sample. The stress dependency of the high-pressure properties is examined with anisotropic elasticity theory from subsequent measurements of energy-dispersive radial diffraction experiments in the diamond-anvil cell. The calculated values of $K_{0T}$ depend largely upon the angle $\psi$ between the diffracting plane normal and the maximum stress axis. The uniaxial stress component in the sample, $t = \sigma_3 - \sigma_1$, varies with pressure as $t = -3.11 + 0.43P$ between 10 and 30 GPa. The pressure derivatives of the elastic moduli $dC_{11}/dP = 5.76$ ($\pm 0.15$), $dC_{12}/dP = 1.41$ ($\pm 0.11$) and $dC_{44}/dP = 1.92$ ($\pm 0.06$) are obtained from the diffraction data assuming previously reported zero-pressure ultrasonic data ($C_{11} = 382$ GPa, $C_{12} = 31$ GPa, and $C_{44} = 109$ GPa).

**Keywords** High pressure · Elasticity · Pyrite · Shear strength · Radial diffraction

S. Merkel · J. Shu · H.-K. Mao · R. J. Hemley
Geophysical Laboratory and Center for High-Pressure Research, Carnegie Institution of Washington, 5251 Broad Branch Rd., NW, Washington DC 20015-1305, USA, e-mail: merkel@gl.ciw.edu

S. Merkel (✉) · P. Gillet
Laboratoire des Sciences de la Terre,
École normale supérieure de Lyon, 46 allée d'Italie,
69364 Lyon Cedex 07, France, e-mail: smerkel@ens-lyon.fr
Tel.: +33-4-72-72-85-66; Fax: +33-4-72-72-86-77

A. P. Jephcoat
Department of Earth Sciences, University of Oxford,
Parks Road, Oxford OX1 3PR, UK

## Introduction

Pyrite crystallizes in the cubic symmetry [space group $T_h^6(Pa3)$] and appears to have a wide stability field. X-ray diffraction experiments, performed up to pressures of 40 GPa, show no evidence of phase transition (Bridgman 1949; Drickamer et al. 1966; Chattopadhyay and Schnering 1985; Jephcoat 1985; Fujii et al. 1986). Moreover, shock compression data demonstrate that pyrite does not undergo any phase transition up to a pressure of at least 320 GPa (Ahrens and Jeanloz 1987). However, the bulk moduli deduced from these experiments show large differences and the results do not agree. Moreover, equation of state (EOS) measurements under nonhydrostatic conditions at high pressure and ambient temperature using X-ray diffraction and the diamond-anvil cell up to pressures of 40 GPa yielded some unusual results: the EOS was found to be very dependent on the experimental stress conditions, with a bulk modulus varying from 130 to 250 GPa with different pressure-transmitting media used in the experiments (Jephcoat 1985). Such variations between the different measurements in the diamond-anvil cell can be explained by the presence of anisotropic stress conditions that differ between experiments. This has been one of the major sources of errors and inconsistencies in the determination of high-pressure properties of materials with diamond-anvil cell experiments. Thus, there is a need to investigate both the high-pressure properties of materials and the stress conditions under which the experimental measurements are performed.

The purpose of this study was to examine the high-pressure properties of pyrite and the conditions under which they are measured in detail using new experimental and theoretical techniques. In particular, we used methods developed to analyze quantitatively lattice strains under nonhydrostatic stress conditions in the diamond-anvil cell (Singh 1993b; Singh et al. 1998a, b). The powdered sample is confined in a diamond cell without a pressure medium to enhance the effects of nonhydrostaticity, and diffraction patterns are measured

through the gasket with several orientations of the X-ray beam. Analyzing the effects of orientation on the measured interplanar $d$ spacings can yield information on shear strength, quasihydrostatic compression curves, elastic moduli, as well as elastic anisotropy. This technique has been applied to iron (Mao et al. 1998; Singh et al. 1998b), gold and rhenium (Duffy et al. 1999a), and molybdenum (Duffy et al. 1999b).

The first section of this paper summarizes previously unpublished X-ray diffraction results on the EOS of pyrite (Jephcoat 1985). Two experiments were performed without a pressure medium, thus under nonhydrostatic stress conditions, and a third experiment hydrostatically with neon as a pressure medium. The EOS were found to be very dependent on the degree of nonhydrostatic stress in the sample. We then describe the theory behind the radial diffraction experiments and how it can be used to deduce physical properties of the sample. Finally, we present results of the radial diffraction experiments and analysis for obtaining hydrostatic compression curve, elasticity, shear strength, and elastic anisotropy of pyrite.

## Conventional diffraction experiments

### Description of the experiments

Three sets of EOS experiments were performed in a diamond-anvil cell using a sealed MoK$\alpha$ ($\lambda = 71.073$ pm) source at the Geophysical Laboratory. The collimated X-ray beam was directed through the diamond anvils, and diffraction patterns were collected with a film camera in Debye–Scherrer geometry (Fig. 1). An extended silver standard was used to calibrate the film to sample distance (Jephcoat et al. 1987). Two runs (NH1 and NH2) were performed nonhydrostatically up to pressures of about 25 and 30 GPa, respectively. A hydrostatic run (NE1) was also performed with solid neon as a pressure medium up to 40 GPa. For all experiments, large single crystals of pure, natural pyrite (Elba, Italy) were ground to a powder in a suspension of ethanol.

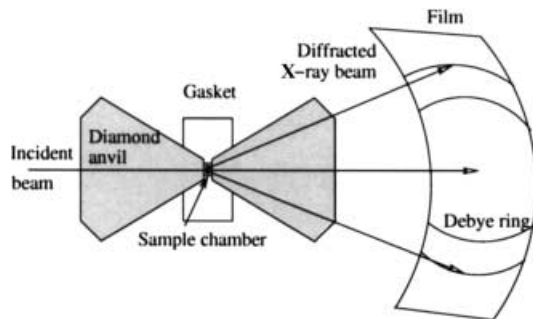For the first experiment (NH1), diamonds with a 550-µm diameter culet were chosen and a 160-µm diameter hole drilled in a T301 steel gasket was used as a sample chamber. The hole was filled with the pyrite powder and covered with a layer of ruby chips before assembling the cell. An asymmetric pressure gradient developed across the diamond face, as opposed to the maximum expected at the culet center. The X-ray photographs showed spotty diffraction rings, suggesting that the sample grain size was too large, and the experiment was stopped at 25 GPa.

For run NE1, the same diamonds were used. The sample was ground for a longer period than in the previous experiment and pressed into a platelet between the piston diamond and a glass microscope slide. A disk was cut from this platelet to a diameter slightly smaller than the hole. Finally, ground ruby was distributed throughout the sample, and pressed lightly into it. Pure neon was then loaded at 0.2 GPa (Jephcoat et al. 1987). Pressures were measured at several points across the sample for averaging at each increment in pressure.

As a result of the large discrepancy between the first two runs (see results in Fig. 2), a second nonhydrostatic compression experiment (NH2) was carried out to check the accuracy of the first (NH1). Larger-culet diamonds (950 µm diameter) were used and a 200-µm hole was drilled in the gasket. The same powdered sample was reground and loaded into the gasket and repeatedly pressed until fully compacted and ground ruby powder was deposited on the surface. Up to nine reflections from the following set of indices were identified manually on the X-ray film: (1 1 1), (2 0 0), (2 1 0), (2 1 1), (2 2 0), (3 1 1), (2 2 2), (2 3 0), and (3 2 1). A zero-pressure lattice constant of 5.417(5) was used.

## Results

Compression data for experiments NE1, NH1, and NH2 are presented in Tables 1, 2, and 3, respectively. Com-
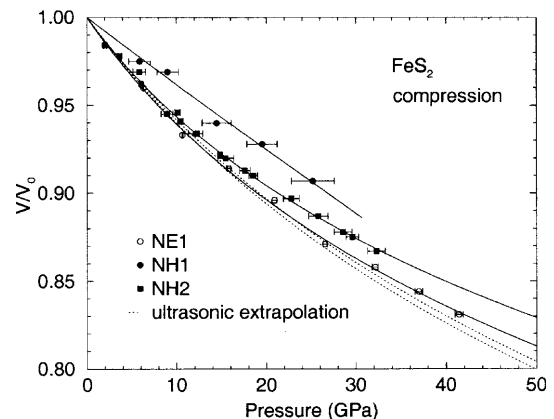


**Fig. 1** Experimental setup for conventional diffraction experiments NE1, NH1, and NH2. A collimated X-ray beam MoK$\alpha$ ($\lambda = 71.073$ pm) passes along the diamond cell load axis and exposes the film held in a camera at fixed radius



**Fig. 2** Compression curves of pyrite: NE1 (*open circles*) with neon as pressure medium, NH1 (*closed circles*), and NH2 (*closed squares*) with no pressure medium. *Solid lines* are third-order Birch–Murnaghan fits to the data and *dotted lines* are extrapolated compression curves from zero-pressure ultrasonic measurements of elastic moduli. (Simmons and Birch 1963)

pression curves derived from these experiments are shown in Fig. 2. The results from compression with neon medium are in reasonably close agreement with expectation on the basis of zero-pressure elastic constant measurements (Simmons and Birch 1963).

Pyrite appears significantly less compressible in the two nonhydrostatic experiments (NH1 and NH2). Although the effect of nonhydrostatic stress in NH1 was reproduced in NH2, its magnitude was not. Possible explanations for the difference in magnitude are (1) that the larger diamond culet surface of run NH2 reduced the pressure gradients and the degree of nonhydrostaticity; and (2) that the sample grain size was smaller for run NH2 (<10 μm). Other factors that distinguished run NH1 and NH2 were a lower concentration of ruby in the surface layer, and a larger sample thickness.

**Table 1** Compression data for $FeS_2$ at 293 K with a neon pressure medium (experiment NE1)

| $P$ (GPa) | $a$ (Å) | $V$ (cm$^3$ mol$^{-1}$) | $V/V_0$ |
|---|---|---|---|
| 6.30 ($\pm$0.01) | 5.344 ($\pm$0.001) | 22.979 ($\pm$0.019) | 0.960 ($\pm$0.001) |
| 10.65 ($\pm$0.06) | 5.294 ($\pm$0.002) | 22.332 ($\pm$0.022) | 0.933 ($\pm$0.001) |
| 15.84 ($\pm$0.15) | 5.257 ($\pm$0.001) | 21.866 ($\pm$0.012) | 0.914 ($\pm$0.001) |
| 20.91 ($\pm$0.27) | 5.222 ($\pm$0.001) | 21.433 ($\pm$0.017) | 0.896 ($\pm$0.001) |
| 26.57 ($\pm$0.24) | 5.173 ($\pm$0.002) | 20.837 ($\pm$0.027) | 0.871 ($\pm$0.001) |
| 32.12 ($\pm$0.34) | 5.146 ($\pm$0.002) | 20.520 ($\pm$0.018) | 0.858 ($\pm$0.001) |
| 36.99 ($\pm$0.42) | 5.119 ($\pm$0.003) | 20.199 ($\pm$0.037) | 0.844 ($\pm$0.002) |
| 41.44 ($\pm$0.42) | 5.094 ($\pm$0.005) | 19.894 ($\pm$0.062) | 0.831 ($\pm$0.003) |

**Table 2** Nonhydrostatic compression data for $FeS_2$ at 293 K (experiment NH1)

| $P$ (GPa) | $a$ (Å) | $V$ (cm$^3$ mol$^{-1}$) | $V/V_0$ |
|---|---|---|---|
| 5.89 ($\pm$1.2) | 5.372 ($\pm$0.004) | 23.333 ($\pm$0.054) | 0.975 ($\pm$0.002) |
| 9.01 ($\pm$1.2) | 5.360 ($\pm$0.001) | 23.188 ($\pm$0.014) | 0.969 ($\pm$0.001) |
| 14.46 ($\pm$1.6) | 5.306 ($\pm$0.005) | 22.492 ($\pm$0.060) | 0.940 ($\pm$0.003) |
| 19.54 ($\pm$1.7) | 5.284 ($\pm$0.002) | 22.216 ($\pm$0.030) | 0.928 ($\pm$0.001) |
| 25.20 ($\pm$2.4) | 5.243 ($\pm$0.003) | 21.695 ($\pm$0.034) | 0.907 ($\pm$0.002) |

**Table 3** Nonhydrostatic compression data for $FeS_2$ at 293 K (experiment NH2)

| $P$ (GPa) | $a$ (Å) | $V$ (cm$^3$ mol$^{-1}$) | $V/V_0$ |
|---|---|---|---|
| 3.68 ($\pm$0.18) | 5.376 ($\pm$0.001) | 23.394 ($\pm$0.012) | 0.978 ($\pm$0.001) |
| 10.10 ($\pm$0.28) | 5.3171 ($\pm$0.004) | 22.632 ($\pm$0.005) | 0.946 ($\pm$0.001) |
| 14.83 ($\pm$0.21) | 5.273 ($\pm$0.002) | 22.072 ($\pm$0.024) | 0.922 ($\pm$0.001) |
| 18.55 ($\pm$0.50) | 5.250 ($\pm$0.002) | 21.786 ($\pm$0.019) | 0.910 ($\pm$0.001) |
| 22.80 ($\pm$0.89) | 5.223 ($\pm$0.002) | 21.455 ($\pm$0.020) | 0.897 ($\pm$0.001) |
| 28.55 ($\pm$1.00) | 5.187 ($\pm$0.001) | 21.013 ($\pm$0.015) | 0.878 ($\pm$0.001) |
| 32.29 ($\pm$1.00) | 5.166 ($\pm$0.002) | 20.752 ($\pm$0.019) | 0.867 ($\pm$0.001) |
| 25.81 ($\pm$1.07) | 5.205 ($\pm$0.001) | 21.233 ($\pm$0.018) | 0.887 ($\pm$0.001) |
| 15.48 ($\pm$0.87) | 5.269 ($\pm$0.002) | 22.023 ($\pm$0.019) | 0.920 ($\pm$0.001) |
| 12.12 ($\pm$0.81) | 5.2957 ($\pm$0.004) | 22.359 ($\pm$0.005) | 0.934 ($\pm$0.001) |
| 8.94 ($\pm$0.67) | 5.317 ($\pm$0.001) | 22.624 ($\pm$0.010) | 0.945 ($\pm$0.001) |
| 6.06 ($\pm$0.16) | 5.348 ($\pm$0.001) | 23.028 ($\pm$0.016) | 0.962 ($\pm$0.001) |
| 2.02 ($\pm$0.17) | 5.388 ($\pm$0.001) | 23.549 ($\pm$0.014) | 0.984 ($\pm$0.001) |
| 5.84 ($\pm$0.70) | 5.360 ($\pm$0.002) | 23.183 ($\pm$0.025) | 0.969 ($\pm$0.001) |
| 12.29 ($\pm$0.14) | 5.295 ($\pm$0.001) | 23.344 ($\pm$0.015) | 0.934 ($\pm$0.001) |
| 10.44 ($\pm$0.30) | 5.307 ($\pm$0.001) | 22.506 ($\pm$0.015) | 0.941 ($\pm$0.001) |
| 17.61 ($\pm$0.60) | 5.255 ($\pm$0.001) | 21.842 ($\pm$0.009) | 0.913 ($\pm$0.001) |
| 29.59 ($\pm$0.69) | 5.182 ($\pm$0.002) | 20.946 ($\pm$0.020) | 0.875 ($\pm$0.001) |

For nonhydrostatic experiment NH2, data were collected by cycling the cell up and down in pressure several times (Table 3). There appear to be no systematic effects attributable to increasing or decreasing pressure cycles within the scatter of the data.

## Discussion

Earlier ultrasonic measurements of zero-pressure elastic moduli by (Simmons and Birch 1963) provide values of $K_{0S}$ ranging from 142.7 to 147.9 GPa, depending on the sample used. Analysis of shock-compression data between 0 and 320 GPa yields $K_{0S} = 162$ ($\pm$9) GPa and $K'_{0S} = 4.7$ ($\pm$0.3) (Ahrens and Jeanloz 1987).

The adiabatic and isothermal bulk moduli can be related using

$$K_S = K_T(1 + \alpha\gamma T) = K_T\left(1 + \frac{\alpha^2 K_S V T}{C_P}\right) , \qquad (1)$$

where $\alpha$ is the volume thermal expansivity, $\gamma$ the thermodynamic Grüneisen parameter, $C_P$ the constant pressure heat capacity, $V$ the unit cell volume, and $T$ the absolute temperature. With $\alpha = 2.6 \times 10^{-5}$ K$^{-1}$, $V = 159.04$ Å$^3$ (Ahrens 1995), $C_P = 62.17$ J $\cdot$ mol$^{-1} \cdot$ K$^{-1}$ (Robie et al. 1979), and $T = 300$ K, we calculate $K_T/K_S \approx 0.988$. Thus $K_S$ and $K_T$ at ambient temperature differ by about 1%, which is within experimental error. Reported measurements of $K_{0T}$ for pyrite using X-ray diffraction include 149.3 and 147.1 GPa (Bridgman 1949) with data up to 0.3 GPa, $K_{0T} = 148$ GPa, and $K'_{0T} = 5.5$ by Drickamer et al. (1966) with data up to 30 GPa, $K_{0T} = 157$ GPa by Fujii et al. (1986) with data up to 4.2 GPa, $K_{0T} = 215$ GPa and $K'_{0T} = 5.5$ by Chattopadhyay and Schnering (1985) with data up to 34 GPa.

A third-order Birch–Murnaghan EOS was fitted to the data for each experiment with $K'_{0T}$ free and $K'_{0T} = 4.0$ (Table 4). Assuming $K'_{0T} = 4.0$, the bulk modulus obtained from the neon medium experiment (NE1), $K_{0T} = 143$ ($\pm$4) GPa, is compatible with the zero-pressure ultrasonic measurements of elastic moduli that lead to $K_{0S} = 145$ ($\pm$3) GPa (Simmons and Birch 1963). Shock-compression data assuming $K'_{0S} = 4.7$ ($\pm$0.3) estimate $K_{0S} = 162$ ($\pm$9), which is approximately 20% larger and well outside the limits of esti-

**Table 4** Birch–Murnaghan EOS parameters for $FeS_2$ at 293 K for experiment with neon as a pressure medium NE1, and nonhydrostatic compressions NH1 and NH2. For each experiment $V_0$ was fixed to its zero-pressure value and parameters of the third-order Birch–Murnaghan EOS were adjusted with $K'_0$ free and $K'_0 = 4.0$

| Dataset | $K_{0T}$ (GPa) | $K'_{0T}$ |
|---|---|---|
| NE1 | 133.5 ($\pm$5.2) | 5.73 ($\pm$0.58) |
| NE1 | 142.8 ($\pm$0.2) | 4.00 |
| NH1 | 255.0 ($\pm$27.0) | 0.5 ($\pm$2.7) |
| NH1 | 224.0 ($\pm$13.1) | 4.00 |
| NH2 | 140.8 ($\pm$3.2) | 7.02 ($\pm$7.4) |
| NH2 | 157.3 ($\pm$1.0) | 4.00 |

mated errors. Thermal correction to the Hugoniot data is less than 20% and does not explain this discrepancy. It could be explained by a small volume increase across a shock-induced transition that could not be induced by pressure alone or by the occurrence of partial fusion during the shock experiment (Ahrens and Jeanloz 1987). In any case, the tradeoffs between $K_0'$ and $K_0$ for different EOS formalisms do not warrant a detailed comparison.

Large differences in the equation-of-state parameters arise when varying the nonhydrostatic stress in experiments NH1 and NH2 and the other experiments obtain results within the wide range of those obtained here (Table 4). It is, therefore, apparent that effects of experimental conditions and nonhydrostatic stress on the compression curve are extremely large in pyrite. Further investigation of the underlying causes of these variations requires knowledge of the elastic properties and the shear strength of the material as well as their pressure dependence. The elastic moduli of pyrite have been studied experimentally at zero pressure (Simmons and Birch 1963), but no study has been conducted to higher pressures. We used newly developed, high-pressure radial diffraction measurements to understand the nature of elasticity and shear strength in pyrite under these conditions.

## Theory of radial diffraction

The theory of lattice strains under nonhydrostatic pressure conditions in the diamond-anvil cell has been described elsewhere (Singh 1993 b; Singh et al. 1998a, b). We present a short summary of the main features. The sample is submitted to uniaxial stress conditions in the diamond cell; the geometry for radial diffraction experiments is shown in Fig. 3. The stress tensor in the sample can be expressed as

**Fig. 3** Experimental setup for radial diffraction. The powdered sample is confined under nonhydrostatic stress between the two diamond anvils without any pressure medium. $\sigma_{3d}$ is the axial stress imposed by the diamonds and $\sigma_{1d}$ the radial stress imposed by the gasket. A layer of pressure calibrant (gold in this case) is added on the top of the sample. The cell is rotated about the axis $R$ between $\psi = 0°$ and $\psi = 90°$ with 15° intervals
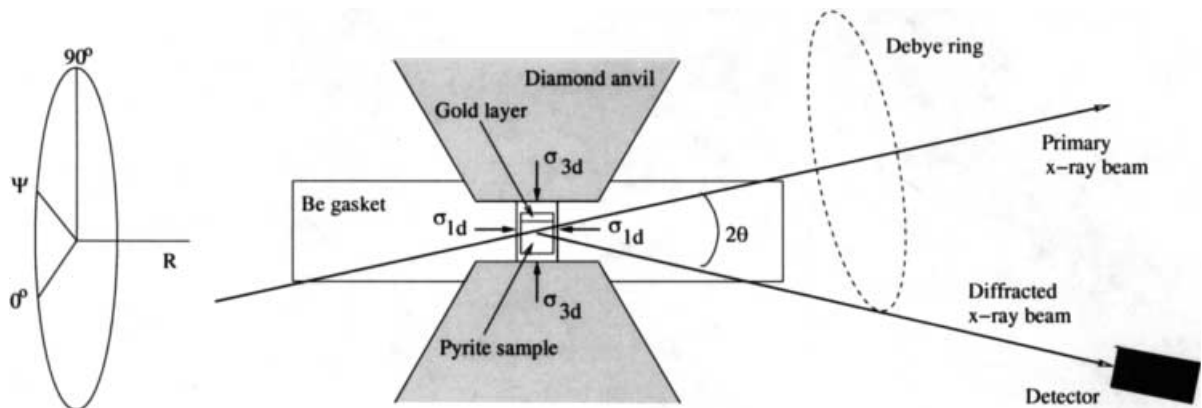
$$
\sigma = \begin{bmatrix} \sigma_1 & 0 & 0 \\ 0 & \sigma_1 & 0 \\ 0 & 0 & \sigma_3 \end{bmatrix}
$$
$$
= \begin{bmatrix} \sigma_P & 0 & 0 \\ 0 & \sigma_P & 0 \\ 0 & 0 & \sigma_P \end{bmatrix} + \begin{bmatrix} -t/3 & 0 & 0 \\ 0 & -t/3 & 0 \\ 0 & 0 & 2t/3 \end{bmatrix} , \quad (2)
$$

where $\sigma_1$ and $\sigma_3$ are the radial and axial stress components, respectively. $\sigma_P$ is the normal mean stress or equivalent hydrostatic pressure. The uniaxial stress component $t = (\sigma_3 - \sigma_1)$ is the deviatoric stress component.

The $d$ spacing for a given set of lattice planes measured by X-ray diffraction is a function of the angle $\psi$ between the principal stress axis of the diamond cell and the diffracting plane normal (see Fig. 4) and can be expressed as:

$$
d_m(hkl) = d_P(hkl)\left[1 + (1 - 3\cos^2\psi)Q(hkl)\right] , \quad (3)
$$

where $d_m(hkl)$ is the measured $d$ spacing and $d_P(hkl)$ the $d$ spacing under the hydrostatic pressure $\sigma_P$. $Q(hkl)$ is given by

$$
Q(hkl) = \frac{t}{3}\left[\frac{\alpha}{2G_R(hkl)} + \frac{1-\alpha}{2G_V}\right] . \quad (4)
$$

$G_R(hkl)$ and $G_V(hkl)$ are the shear moduli of the aggregate under the Reuss (iso-stress) and Voigt (iso-strain) approximations, respectively, and are not orientation-dependent. The factor $\alpha$, which lies between 0 and 1, determines the relative weight of iso-stress (Reuss) and iso-strain (Voigt) conditions. It specifies the degree of stress and strain continuity across grains in the sample.

For a cubic system, we have

$$
(2G_V)^{-1} = \frac{5}{2}\frac{(S_{11} - S_{12})S_{44}}{[3(S_{11} - S_{12}) + S_{44}]} \quad (5)
$$

and

$$
(2G_R)^{-1} = S_{11} - S_{12} - 3S\Gamma(hkl) , \quad (6)
$$

where

$$
S = S_{11} - S_{12} - S_{44}/2 \quad (7)
$$

and

$$\Gamma(hkl) = \frac{h^2k^2 + k^2l^2 + l^2h^2}{(h^2 + k^2 + l^2)^2} \quad . \tag{8}$$

The $S_{ij}$ are the single-crystal elastic compliances; $S$ is a measure of elastic anisotropy.

According to Eq. (3), $d_m(hkl)$ should vary linearly with $(1 - 3\cos^2\psi)$. The intercept ($\psi = 54.7°$) yields $d_P(hkl)$, the $d$ spacing due to the hydrostatic component of the stress, and the slope the product $d_P(hkl)Q(hkl)$.

Equations (4–6) imply a linear relationship between $Q(hkl)$ and $3\Gamma(hkl)$ with intercept $m_0$ and slope $m_1$ given by

$$m_0 = \frac{t}{3}\left[\alpha(S_{11} - S_{12}) + (1 - \alpha)\frac{5}{2}\frac{(S_{11} - S_{12})S_{44}}{[3(S_{11} - S_{12}) + S_{44}]}\right] \tag{9}$$

$$m_1 = -\frac{\alpha t}{3}[S_{11} - S_{12} - S_{44}/2] \quad . \tag{10}$$

The bulk modulus $K$ is defined by

$$K_T = -V\left(\frac{\partial p}{\partial V}\right)_T = \frac{1}{3[S_{11} + 2S_{12}]} \quad . \tag{11}$$

Estimating the nonhydrostatic stress in the sample $t$ using the relation (Singh 1993a; Singh et al. 1998a)

$$t = 6G\langle Q(hkl)\rangle \quad , \tag{12}$$

we have enough information to deduce the three elastic compliances $S_{11}$, $S_{12}$, and $S_{44}$ of a cubic material that can be inverted to the three independent elastic stiffnesses $C_{11}$, $C_{12}$, and $C_{44}$.

## Radial diffraction experiment

### Experimental technique

Sample preparation was similar to previous experiments NE1 and NH2. The sample consisted of a fine-grained pyrite powder with a thin layer of gold powder on one face contained in a 50-μm diameter hole drilled in a beryllium gasket. The absence of pressure transmitting medium enhances the effects of nonhydrosticity. Diamonds with a 300-μm diameter culet were used.

The experiment was conducted using energy-dispersive synchrotron X-ray diffraction at the NSLS Synchrotron National Source, beam line X-17C, and data were collected using a germanium solid-state detector set at a fixed angle with respect to the incident beam. Compression was performed using a diamond-anvil cell mounted on a rotating stage. The angle $\psi$ between the diffraction plane normal and the diamond-anvil cell stress axis varied between 0° and 90° with 15° intervals (Fig. 3). We performed measurements for six pressure points at 5.6, 13.2, 20.5, 29.0, 36.5, and 47.8 GPa. Hydrostatic pressures were determined from the deduced lattice parameter at $\psi = 54.7°$ and the EOS of gold (Heinz and Jeanloz 1984).

The analysis on gold was based on the (1 1 1), (2 0 0), and (2 2 0) diffraction lines. For pyrite, we used the

positions of the reflections (1 1 1), (2 0 0), (2 2 0), (2 1 1), (2 3 0), and (2 2 2). Diffraction lines were fitted to Voigtian peaks with varying height and width. As in the previous experiments, a diffraction line was rejected if there was unusually large error as a result of low intensity or overlap problems between gold, beryllium, or pyrite lines.

### Radial diffraction equation of state

Figure 5 shows a typical set of diffraction patterns. A shift of the diffraction lines toward lower energies with increasing $\psi$ angle can be observed. For $\psi = 90°$, the diffracting planes are aligned with the minimum stress axis, resulting in maximum $d$ spacings. At $\psi = 0°$, the diffracting planes are orthogonal to the maximum stress axis, resulting in minimum $d$ spacings (Figs. 4 and 6).

The variations of the peak positions with the $\psi$ angle for pyrite are shown in Fig. 6 for the (1 1 1) and (2 0 0)
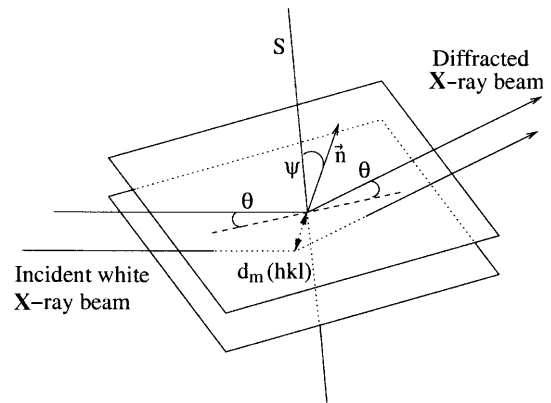


**Fig. 4** For a given $\psi$ angle between the diffracting plane normal $\vec{n}$ and the maximum stress axis $S$, we measure a $d$ spacing $d_m(hkl)$ function of the Miller indices $h$, $k$, and $l$, but also the angle $\psi$ because of the nonhydrostatic compression. When $\psi = 0°$, the diffracting plane is orthogonal with the maximum stress axis $S$, thus $d_m(hkl)$ is minimum. When $\psi = 90°$, the diffracting plane is aligned with the maximum stress axis $S$, thus $d_m(hkl)$ is maximum
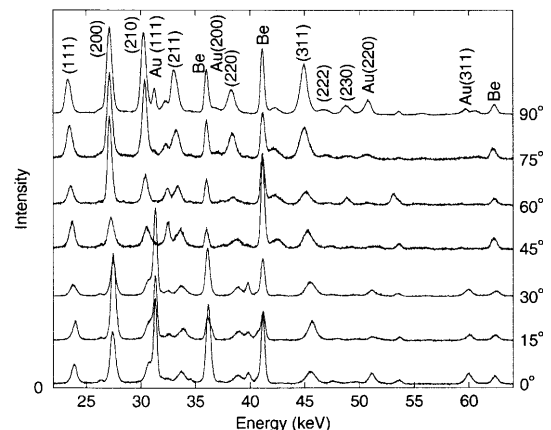


**Fig. 5** X-ray diffraction patterns as a function of $\psi$ angle for $P = 20.5$ GPa. Diffraction lines from pyrite, gold, and beryllium are *labeled*. The shift of the peak positions with the $\psi$ angle can be observed; for example, pyrite (1 1 1)

reflections for different pressures. As predicted from Eq. (3), a linear dependence is observed between $d_m(hkl)$ and $(1 - 3\cos^2\psi)$. The lattice parameters under equivalent hydrostatic pressures can be deduced from the $d$ spacings at the "magic angle" ($\psi = 54.7°$). The pyrite unit-cell volumes deduced from these measurements are presented in Table 5 and Fig. 7.

Compression curves are presented in Fig. 7, calculated for $\psi = 0°$, $\psi = 54.7°$, and $\psi = 90°$. For each pressure, we observe very large variation of the unit-cell volume with the $\psi$ angle (Table 5). This is in agreement with the results from experiments NE1, NH1, and NH2, which showed that EOS measurement was very dependent on the stress conditions in the sample. Third-order, Birch–Murnaghan EOS fit parameters for the data in Fig. 7 are presented in Table 6. The difference between the bulk moduli calculated at $\psi = 0°$ and $\psi = 90°$ is about 45%, showing the very large effect of the nonhydrostatic stress on the EOS of pyrite. Assuming that $K'_{0T} = 4.0$, $K_{0T}$ ranges from 121 GPa for $\psi = 0°$ to 193 GPa for $\psi = 90°$. These values are consistent with results from experiments NH2 (Table 4). Results from experiment NH1 are quite different, but could be explained by the scatter in the data and effects due to the larger grain size. Our deduced hydrostatic curve ($\psi = 54.7°$) is in good agreement with previous hydrostatic measurements from experiment NE1. Assuming $K'_{0T} = 4.0$, we obtain $K_{0T} = 156$ GPa, compared to
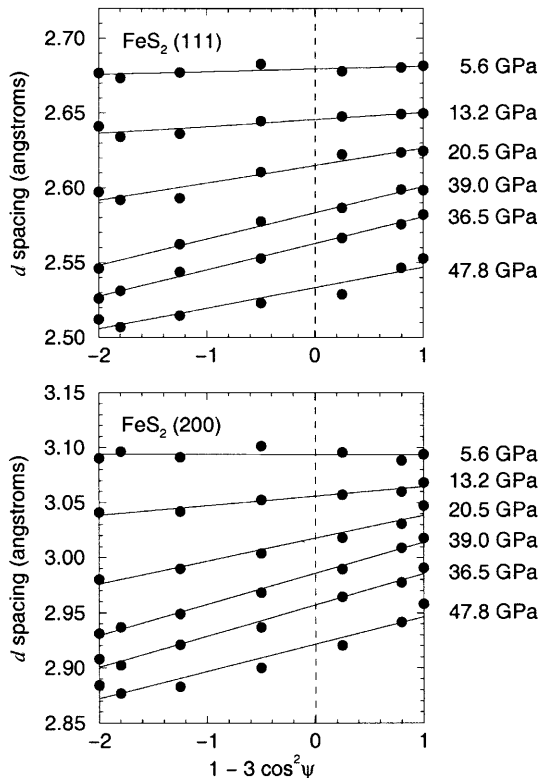
$K_{0T} = 143$ GPa for NE1. It is therefore possible to measure a hydrostatic EOS under these very nonhydrostatic conditions by choosing the right orientation of the diffraction vector.

## Yield strength of pyrite

From the least-squares lines in Fig. 6, using Eq. (3) we can calculate $Q(hkl)$ for each observed reflection and pressure. For each pressure $Q(hkl)$ should vary linearly

**Table 5** Unit-cell volume of pyrite as a function of pressure deduced from the radial diffraction experiment at 293 K. We indicate results from measurements at different $\psi$ angle. The volume under equivalent hydrostatic stress is calculated for $\psi = 54.7°$

| $P$ (GPa) | $V/V_0$ at $\psi = 0°$ | $V/V_0$ at $\psi = 90°$ | $V/V_0$ at $\psi = 54.7°$ |
|---|---|---|---|
| 5.6 | 0.9659 ($\pm 0.007$) | 0.9676 ($\pm 0.013$) | 0.9676 ($\pm 0.003$) |
| 13.2 | 0.9184 ($\pm 0.046$) | 0.9384 ($\pm 0.016$) | 0.9303 ($\pm 0.005$) |
| 20.5 | 0.8734 ($\pm 0.037$) | 0.9169 ($\pm 0.045$) | 0.8984 ($\pm 0.002$) |
| 29.0 | 0.8265 ($\pm 0.063$) | 0.8908 ($\pm 0.038$) | 0.8684 ($\pm 0.007$) |
| 36.5 | 0.8064 ($\pm 0.035$) | 0.8657 ($\pm 0.019$) | 0.8441 ($\pm 0.031$) |
| 47.8 | 0.7891 ($\pm 0.039$) | 0.8420 ($\pm 0.025$) | 0.8166 ($\pm 0.005$) |



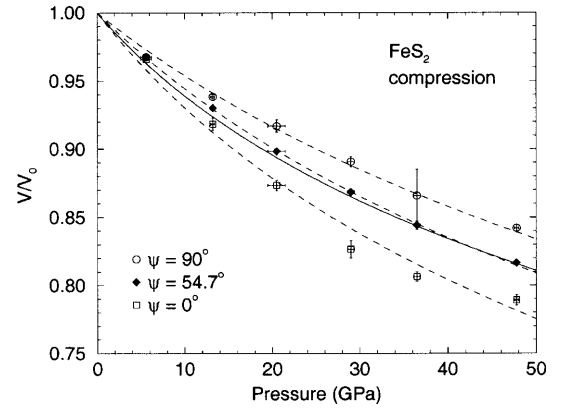**Fig. 7** EOS of pyrite measured at $\psi = 0°$, $\psi = 54.7°$ and $\psi = 90°$. Pressure is calibrated according to the hydrostatic EOS of gold (Heinz and Jeanloz 1984). *Dashed lines* are Birch–Murnaghan fits to the data. *Solid line* corresponds to the previous hydrostatic EOS measured in a neon medium from experiment NE1. Large differences appear between the EOS at different $\psi$ angles, resulting from large nonhydrostatic stress in pyrite



**Fig. 6** Dependence of the $d$ spacing on $\psi$ for selected pyrite diffraction lines and different pressures. *Solid lines* are least-squares fits to the data. *Dashed lines* indicate the angle $\psi$ where the measured $d$ spacing corresponds to the $d$ spacing under equivalent hydrostatic pressure

**Table 6** Birch–Murnagham EOS parameters for FeS$_2$ at 293 K for the radial diffraction experiment. Results are given for different $\psi$ angles, including $\psi = 54.7°$, where the volume measured is the volume under an equivalent hydrostatic stress. For each case $V_0$ was fixed to its zero-pressure value and parameters of the third-order Birch–Murnaghan EOS were adjusted with $K'_0$ free and $K'_0 = 4.0$

| $\psi$ | $K_{0T}$ (GPa) | $K'_{0T}$ |
|---|---|---|
| 0° | 116.7 ($\pm 1.1$) | 4.30 ($\pm 0.08$) |
| 0° | 120.8 ($\pm 0.2$) | 4.00 |
| 54.7° | 160.8 ($\pm 5.2$) | 3.50 ($\pm 0.48$) |
| 54.7° | 155.9 ($\pm 1.6$) | 4.00 |
| 90° | 186.6 ($\pm 1.4$) | 4.43 ($\pm 0.09$) |
| 90° | 193.4 ($\pm 0.3$) | 4.00 |

with $\Gamma(hkl)$ (Eqs. 4–8) (Singh 1993b). Figure 8 shows an example of the patterns we observed for three different pressures, 5.6, 13.2, and 20.5 GPa. The experimental data confirm the linear relationship between $Q(hkl)$ and $\Gamma(hkl)$ predicted by theory.

The uniaxial stress component $t$ was calculated using Eq. (12) and least-squares fits shown in Fig. 8 from the relation

$$t = 6G\langle Q(hkl)\rangle = 6G\left(m_0 + \frac{3m_1}{5}\right) , \qquad (13)$$

where $m_0$ and $m_1$ are the intercept and slope from the least-squares fits. The shear modulus of pyrite and its variation with pressure were estimated using $G_0 = 126$ GPa (Simmons and Birch 1963) and assuming a constant $K/G$ ratio as has been done previously (Singh et al. 1998a, b). This approximation is valid over moderate compression (and at temperatures well below melting) for a variety of materials where the pressure dependence of $K$ and $G$ have been measured separately. Nevertheless, the approximation is likely to be the largest source of error in the determination of the high-pressure elastic moduli. $K$ was evaluated along the compression curve from the EOS. Alternatively, an extrapolation of the shear modulus $G$ based on finite strain theory may be used (Davies and Dziewonski 1975). However, this requires knowledge of pressure derivatives of the shear modulus, which have not been measured for pyrite. The calculated variation of $t$ as a function of $P$ is presented in Fig. 9.

At $P = 5.6$ GPa, the nonhydrostatic stress $t$ is very close to zero. We cannot ensure that the stress conditions are really purely uniaxial, as considered in the theory, thus, the theory to deduce the elastic moduli will not be usable because of inappropriate experimental conditions. For higher loads, the observed uniaxial stress component $t$ is larger than previous measurements on gold, molybdenum, and rhenium (Duffy et al. 1999a, b). A linear fit through the data in Fig. 9 between 10 and 30 GPa (where the variation of $t$ is linear with pressure)

leads to the relation $t = -3.11 + 0.43P$, where $P$ is the pressure in GPa, compared to $t = 0.06 + 0.015P$ for gold (Duffy et al. 1999b), $t = 0.46 + 0.13P$ for molybdenum (Duffy et al. 1999b), and $t = 2.5 + 0.09P$ for rhenium (Duffy et al. 1999a). At $P > 30$ GPa, we observe a saturation. This can be explained by the elastic deformations of the diamond anvils that start at this pressure for this geometry (300-µm tip diameter), as investigated by X-ray diffraction and finite-element modeling (Hemley et al. 1997; Merkel et al. 1999, 2000b).

The maximum uniaxial stress $t$ supported by a material is determined by its yield strength; that is $t \leq \sigma_y$, where $\sigma_y$ is the material yield strength. The uniaxial stress $t$ varies with sample environment, and there is equality only if the sample deforms plastically under pressure. Therefore, we conclude that for pyrite

$$\sigma_y \geq -3.11 + 0.43P \qquad (14)$$

between 10 and 30 GPa, where $P$ and $\sigma_y$ are in GPa. This value for the uniaxial stress in pyrite is larger than observations on gold, rhenium, molybdenum (Duffy et al. 1999a), iron, FeO (Singh et al. 1998b), and tungsten (Hemley et al. 1997).

## Elasticity

Using Eqs. (9–11) we can calculate the single-crystal elastic moduli of the sample. Results for the iso-stress hypothesis ($\alpha = 1$) and for $\alpha = 0.5$ are presented in Tables 7 and 8, respectively. The elastic stiffnesses calculated for $\alpha = 0.5$ do not match the zero-pressure ultrasonic measurements $C_{11} = 381.8$ GPa, $C_{12} = 31.0$ GPa and $C_{44} = 109.4$ GPa (Simmons and Birch 1963). On the other hand, the results for $\alpha = 1$ (the iso-stress hypothesis, Table 7) seem to be in good agreement: Fig. 10 shows the elastic stiffnesses calculated for $\alpha = 1$ and the zero-pressure ultrasonic data. We performed a linear fit through the X-ray data to evaluate the first pressure derivative of the $C_{ij}$s. We find
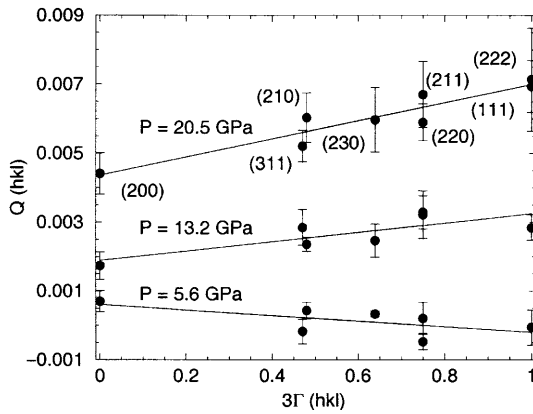


**Fig. 8** $Q(hkl)$ vs. $3\Gamma(hkl)$ for pyrite at $P = 5.6$, 13.2, and 20.5 GPa. The *solid lines* are least-squares fits to the data. Errors on $Q(hkl)$ are estimated with the scatter of the $d(hkl)$ vs. $\psi$ relation. *Error bars* represent $2\sigma(Q)$
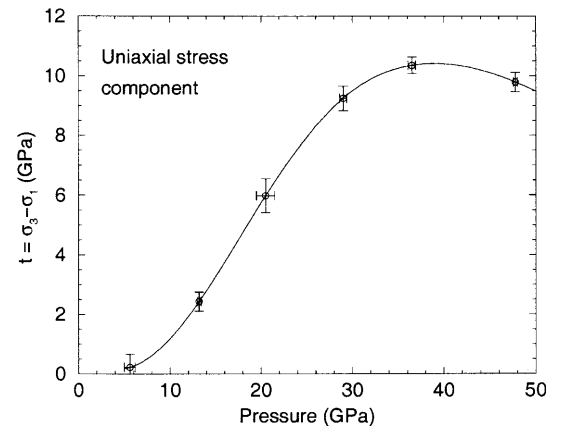
**Fig. 9** Uniaxial stress component $t = \sigma_3 - \sigma_1$ in the sample vs. pressure. *Solid line* is a cubic spline through the data. The saturation above 30 GPa can be explained by the bending of the diamond anvils

$$\frac{dC_{11}}{dP} = 5.76 \; (\pm 0.15) \tag{15}$$

$$\frac{dC_{12}}{dP} = 1.41 \; (\pm 0.11) \tag{16}$$

$$\frac{dC_{44}}{dP} = 1.92 \; (\pm 0.06) \; . \tag{17}$$

Anisotropy and influence of the $\alpha$ parameter

The elastic anisotropy of a cubic crystal can be characterized by the Zener ratio $A$, which is the ratio of the shear moduli in the (1 0 0) and (1 1 0) planes in the [1 0 0] direction:

$$A = \frac{2C_{44}}{C_{11} - C_{12}} = \frac{2S_{11} - S_{12}}{S_{44}} \; . \tag{18}$$

Assuming $\alpha = 1$ in Eq. (9), we have

$$A = \frac{1}{1 + m_1/m_0} \; . \tag{19}$$

Using the results from our measurements, we find $A$ varying between 0.58 and 0.73 between $P = 13$ GPa and $P = 48$ GPa with $\bar{A} = 0.66$ as average value. This is of the same order as the value at $P = 0$, $A_0 = 0.624$. These results differ strongly from the results on gold from Duffy et al. (1999a), where the apparent $A$ was observed to drop from 2.9 at $P = 0$ to 1.8 at higher pressures when $\alpha = 1$.

Finally, we can study in more detail the influence of the $\alpha$ parameter, which specifies the degree of stress and strain continuity within the sample (Eq. 4), on the elastic moduli. To match the zero-pressure ultrasonic measurements of the elastic moduli, we had to assume $\alpha = 1.0$ (iso-stress hypothesis). The influence of $\alpha$ on the elastic moduli we calculate is presented in Fig. 11 for $P = 20.5$ GPa. All elastic moduli vary quite drastically when $\alpha$ is varied from 0 to 1: $C_{11}$ is found to decrease with increasing $\alpha$, while $C_{12}$
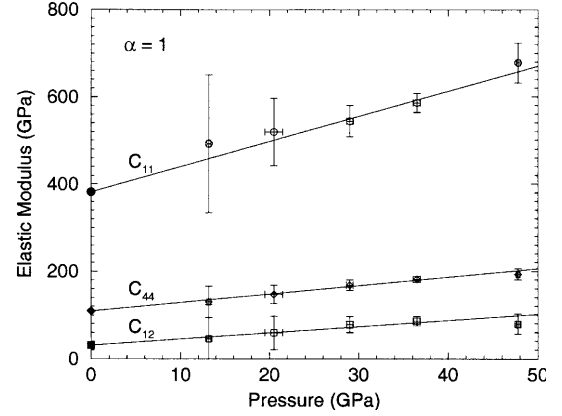


**Fig. 10** Elastic moduli of pyrite and their variations with pressure calculated with $\alpha = 1.0$ (iso-stress condition). *Circles*, *squares*, and *diamonds* are $C_{11}$, $C_{12}$, and $C_{44}$, respectively. *Solid symbols* are zero-pressure ultrasonic measurements (Simmons and Birch 1963), and *open symbols* are deduced from the present experiment. *Lines* are least-squares fits of the first pressure derivatives of the elastic moduli to the data
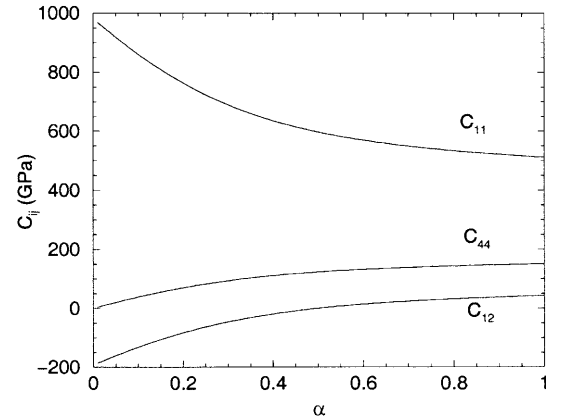


**Fig. 11** Elastic moduli of pyrite at $P = 20.5$ GPa and their variations when calculated with different $\alpha$ parameter

and $C_{44}$ increase. Again, this variation is opposite to the behavior observed in gold (Duffy et al. 1999a).

## Discussion and conclusions

We find the apparent compression curve of pyrite to be very dependent upon the conditions under which the experiment is performed, i.e., shock compression, conventional X-ray diffraction using the diamond-anvil cell and different pressure-transmitting media, or radial X-ray diffraction studies. Application of the technique of radial diffraction made possible an analysis of the nature of these discrepancies. The EOS measured at extreme $\psi$ angles 0° and 90° provide values for the bulk modulus [$K_{0T}(0°) = 121$ GPa and $K_{0T}(90°) = 193$ GPa, assuming $K'_{0T} = 4.0$] between which extremes most previously published experimental results lie.

The hydrostatic EOS measured in the conventional diffraction (along the load axis) experiment (NE1) and

**Table 7** Elastic moduli of pyrite at different pressures calculated for $\alpha = 1$ (iso-stress hypothesis)

| $P$ (GPa) | $\sigma(P)$ | $C_{11}$ (GPa) | $\sigma(C_{11})$ | $C_{12}$ (GPa) | $\sigma(C_{12})$ | $C_{44}$ (GPa) | $\sigma(C_{44})$ |
|---|---|---|---|---|---|---|---|
| 13.2 | 0.2 | 492 | 158 | 45 | 79 | 130 | 36 |
| 20.5 | 1.0 | 519 | 77 | 59 | 38 | 147 | 21 |
| 29.0 | 0.4 | 544 | 36 | 78 | 18 | 168 | 12 |
| 36.5 | 0.4 | 586 | 22 | 86 | 11 | 182 | 7 |
| 47.8 | 0.2 | 678 | 46 | 79 | 23 | 193 | 13 |

**Table 8** Elastic moduli of pyrite at different pressures calculated for $\alpha = 0.5$

| $P$ (GPa) | $\sigma(P)$ | $C_{11}$ (GPa) | $\sigma(C_{11})$ | $C_{12}$ (GPa) | $\sigma(C_{12})$ | $C_{44}$ (GPa) | $\sigma(C_{44})$ |
|---|---|---|---|---|---|---|---|
| 13.2 | 0.2 | 588 | 474 | -3 | 237 | 102 | 36 |
| 20.5 | 1.0 | 602 | 218 | 18 | 109 | 120 | 23 |
| 29.0 | 0.4 | 608 | 92 | 47 | 46 | 145 | 15 |
| 36.5 | 0.4 | 652 | 56 | 53 | 28 | 158 | 10 |
| 47.8 | 0.2 | 785 | 131 | 26 | 65 | 159 | 14 |

that deduced from the radial diffraction experiment at the magic angle are within error. In the experiment with pyrite and ruby confined in solid neon, which is known to be a good hydrostatic medium, the stress condition in the sample chamber can be considered as homogeneous and the pressure deduced from the ruby shift equal to the pressure in the sample. In the radial diffraction experiment, we used the pressure in the gold layer as reference, but there could be differences between the pressure in the gold layer and the sample for two reasons: (1) nonhydrostatic stress is different in gold and pyrite, and (2) the Reuss (iso-stress) conditions between different materials are not completely verified in these kinds of experiments (Duffy et al. 1999b). Thus, small deviations are expected between the deduced pressure and the actual pressure present in the sample. In general, hydrostatic compression is less prone to error; therefore, we conclude that the third-order Birch–Murnaghan EOS parameters for pyrite are $K_{0T} = 133.5$ ($\pm 5.2$) GPa and $K'_{0T} = 5.73$ ($\pm 0.58$).

Further analysis on the results of the radial diffraction experiments indicates the presence of very large uniaxial stress in the sample, implying a very large shear strength for pyrite under high pressure. Thus, differences between EOS measured under different stress conditions are expected since the dependence of the compression curve on nonhydrostatic stress increases with increasing sample shear strength. This can be related to the cases where the compression curve was found to vary between different experiments, making it quite difficult to deduce the bulk modulus and its first pressure derivative. This was observed, for instance, in $MgCO_3$ by (Fiquet and Reynard 1999).

Finally, we have constrained the elastic moduli of pyrite up to 50 GPa and find them to depend linearly on pressure. This study confirms the accuracy of the radial diffraction method to study elastic moduli and strength of material of cubic symmetry under very high pressure. Extension to lower symmetry materials requires further theoretical developments (Merkel et al. 2000a; Wenk et al. 2000).

## References

Ahrens TJ (ed) (1995) Mineral physics and crystallography, a handbook of physical constants. American Geophysical Union, Washington DC

Ahrens TJ, Jeanloz R (1987) Pyrite: shock compression, isentropic release, and the composition of the Earth's core. J Geophys Res 92: 10363–10375

Bridgman PW (1949) Linear compression to 30000 kg/cm$^2$, including relatively incompressible substances. Proc Am Acad Arts Sci 77: 189–234

Chattopadhyay T, Schnering HG von (1985) High-pressure X-ray diffraction study on $p$-$FeS_2$, $m$-$FeS_2$ and $MsS_2$ to 340 kbar: a possible high spin–low spin transition in $MnS_2$. J Phys Chem Sol 46: 113–116

Davies GF, Dziewonski AM (1975) Homogeneity and constitution of the Earth's lower mantle and outer core. Phys Earth Planet Inter 10: 336–343

Drickamer HG, Lynch RW, Clendenen RL, Perez-Albuene EA (1966) X-ray diffraction studies of the lattice parameters of solids under very high pressure. Sol State Phys 19: 135–229

Duffy TS, Shen G, Heinz DL, Shu J, Ma Y, Mao HK, Hemley RJ, Singh AK (1999a) Lattice strains in gold and rhenium under non-hydrostatic compression to 37 GPa. Phys Rev (B) 60: 1–10

Duffy TS, Shen G, Shu J, Mao HK, Hemley RJ, Singh AK (1999b) Elasticity, shear strength and equation of state of molybdenum and gold from X-ray diffraction under nonhydrostatic compression to 24 GPa. J Appl Phys 86: 1–8

Fiquet G, Reynard B (1999) High-pressure equation of state of magnesite: new data and reappraisal. Am Mineral 84: 856–860

Fujii T, Yoshida A, Tanaka K, Marumo F, Nodo Y (1986) High-pressure compressiblities of pyrite and cattierite. Mineral J 13: 202–211

Heinz DL, Jeanloz R (1984) The equation of state of the gold calibration standard. J Appl Phys 55: 885–893

Hemley RJ, Mao HK, Shen G, Badro J, Gillet P, Hanfland M, Häusermann D (1997) X-ray imaging of stress and strain of diamond, iron, and tungsten at megabar pressures. Science 276: 1242–1245

Jephcoat AP (1985) Hydrostatic compression studies on iron and pyrite to high pressures: the composition of the Earth's core and the equation of state of solid argon. PhD Thesis, John Hopkins Univ., Baltimore, Maryland

Jephcoat AP, Mao HK, Bell PM (1987) Operation of the megabar diamond-anvil cell. In: Ulmes GC, Barnes HL, (eds) Hydrothermal experimental techniques. Wiley-Interscience, Wiley, New York

Mao HK, Shu J, Shen G, Hemley RJ, Li B, Singh AK (1998) Elasticity and rheology of iron above 220 GPa and the nature of the Earth's inner core. Nature 396: 741–743. Correction: Nature 399: 280 (1999)

Merkel S, Hemley RJ, Mao HK (1999) Finite-element modeling of diamond deformation at multimegabar pressures. Appl Phys Lett 74: 656–658

Merkel S, Goncharov AF, Mao HK, Gillet P, Hemley RJ (2000a) Raman spectroscopy of iron to 152 gigapascals: implications for Earth's inner core. Science 288: 1626–1629

Merkel S, Hemley RJ, Mao HK, Teter DM (2000b) Finite-element modeling and ab-initio calculations of megabar stresses in the diamond-anvil cell. In: Magnhnani M (ed) Science and technology of high-pressure. University Press (Hydergula, India): 68–73

Robie RA, Hemingway BS, Fisher JR (1979) Thermodynamic porperties of minerals and related substances at 298.15 K and 1 bar ($10^5$ Pascals) pressure and at higher temperatures). US Geol Surv Bull, No. 1452, US Government Printing Office, Washington DC

Simmons G, Birch F (1963) Elastic constants of pyrite. J Appl Phys 34: 2736–2738

Singh AK (1993a) Analysis of $C_{60}$ fullerite compression under non-hydrostatic pressure. Philosoph Mag Lett 67: 379–384

Singh AK (1993b) The lattice strains in a specimen (cubic system) compressed nonhydrostatically in an opposed anvil device. J Appl Phys 73: 4278–4286

Singh AK, Balasingh C, Mao HK, Hemley RJ, Shu J (1998a) Analysis of lattice strains measured under non-hydrostatic pressure. J Appl Phys 83: 7567–7575

Singh AK, Mao HK, Shu J, Hemley RJ (1998b) Estimation of single-crystal elastic moduli from polycrystalline X-ray diffraction at high pressure: applications to FeO and iron. Phys Rev Lett 80: 2157–2160

Wenk HR, Matthies S, Hemley RJ, Mao HK, Shu J (2000) The plastic deformation of iron at pressures of the Earth's inner core. Nature 405: 1044–1047